Petroleum Science 23 (2026) 4414–4429

Contents lists available at ScienceDirect

Petroleum Science

journal homepage: www.keaipublishing.com/en/journals/petroleum-science

Original Paper

Numerical investigation of the effect of reactive transport in rock matrix on fracture fluid flow and heat transfer behavior in enhanced geothermal systems

Jia-Yan Ji [a], Hui Wu [a,b,*], Xian-Zhi Song [c]

[a] School of Earth and Space Sciences, Peking University, Beijing, 100871, China
[b] Peking University Ordos Research Institute of Energy, Ordos, 017010, Inner Mongolia, China
[c] State Key Laboratory of Petroleum Resources and Engineering, China University of Petroleum (Beijing), Beijing, 102249, China

ARTICLE INFO

Article history:
Received 15 October 2025
Received in revised form
11 December 2025
Accepted 28 January 2026
Available online 3 February 2026

Edited by Min Li

Keywords:
Enhanced geothermal system
Reactive transport
Matrix and fracture
Thermal performance
THC coupling model

ABSTRACT

Quantitatively understanding reactive transport in matrix-fracture systems and the corresponding effect on reservoir fluid flow and heat transfer behavior is essential for the prediction of long-term thermal performance in enhanced geothermal systems (EGSs). However, most previous studies on EGSs only considered fracture reactive transport, overlooking matrix reactive transport and its potential impact on fracture flow and reactive transport. In this study, we develop a thermal-hydraulic-chemical coupled EGS model incorporating both fracture and matrix reactive transport to comprehensively investigate the effect of matrix reactive transport on the long-term thermal performance of the EGS model. We find that matrix reactive transport intensifies exchange fluxes between fracture and matrix, thus weakening water-rock reactions in fracture and suppressing fracture deformation, and ultimately improves thermal performance. The modeling results reveal that fracture aperture increment is overestimated by 67 times and the production lifespan is underestimated by 17 years if matrix reactive transport is ignored. Further dimensionless analyses indicate that the significance of matrix reactive transport increases with reaction rate and declines with porosity/permeability when the Damkohler number (*Da*) is less than one (reaction-limited). In EGS and karst reservoirs, matrix reactive transport markedly influences heat extraction efficiency, whereas its effect is negligible in sandstone reservoirs in this study.

1. Introduction

Geothermal energy, as a renewable and clean resource, plays a crucial role in optimizing energy structure, reducing greenhouse gas emissions, and advancing environmental sustainability (Wang et al. 2018). Most of the earth's geothermal resources are stored in hot dry rocks (HDRs), which are generally 3 km or deeper below the ground surface and characterized by high temperature and low permeability (Zhu et al. 2015; Lu, 2018; Anderson and Rezaie, 2019). Enhanced Geothermal System (EGS) is a widely explored technique to harness geothermal energy in HDRs, which applies hydraulic stimulation or shear stimulation to create a hydraulically connected fracture network for fluid circulation and heat extraction (Xu et al. 2018).

The injection of relatively cold working fluid into an EGS reservoir leads to complex thermal-hydraulic-mechanical-chemical (THMC) coupled processes in the stimulated fracture networks as well as the surrounding rock formations (Li et al. 2022; Song et al. 2024), thus changing the thermodynamic, stress, and chemical equilibrium within the reservoir. The induced stress variation and water-rock reactions further alter the porosity and permeability of rock formations, and consequently affect long-term fluid flow and heat transfer performance (Song et al. 2022a). Therefore, it is crucial to investigate how the induced stress changes (He et al. 2025a) and water-rock reactions govern the evolution of fluid flow and heat transfer behavior for accurate prediction of EGS productivity (He et al. 2025b). Numerous thermal-hydraulic-mechanical (THM) coupled models have been developed to analyze the effect of stress changes on fracture flow

* Corresponding author.
E-mail address: hui.wu@pku.edu.cn (H. Wu).

Peer review under the responsibility of China University of Petroleum (Beijing).

https://doi.org/10.1016/j.petsci.2026.01.047

behavior and long-term thermal performance (Pandey et al. 2017; Wang et al. 2019, 2022; Ye and Wang, 2020; Li et al. 2021; Maedo et al. 2021; Kang et al. 2022; He et al. 2024). Both poroelasticity (Wang et al. 2019, 2022; Ye and Wang, 2020; Maedo et al. 2021) and thermoelasticity (Pandey et al. 2017; Li et al. 2021; Kang et al. 2022) have been demonstrated to have significant impacts on fracture deformation and the underlying fluid flow-heat transport behavior.

To understand the effect of water-rock reactions, several thermal-hydraulic-chemical (THC) coupled models have been developed (Lyu et al. 2025). These THC models can be categorized into two primary groups. One group employs continuum models and focuses on the evolution of macroscopic porosity/permeability caused by water-rock reactions, as well as the corresponding effect on heat extraction efficiency (Ontoy et al. 2003; Xu et al. 2004, 2007). The other group adopts discrete fracture network models to analyze the evolution of fracture aperture due to water-rock reactions (Pandey et al. 2015; Chen et al. 2018; Song et al. 2022b). Continuum models reduce the complexity of meshing and have a wide range of applications. For example, Ontoy et al. (2003) and Xu et al. (2004) employed the TOUGHREACT software to develop a THC coupled model based on continuum models and found that precipitation reactions occurred near the injection wells, reducing porosity and permeability and leading to a rapid increase in injection pressure. However, for enhanced geothermal systems, fractures serve as the primary flow pathways. Discrete fracture network models can represent real fracture morphology and characterize fluid flow, heat transfer and other processes in reservoirs more accurately than continuum models. Therefore, discrete fracture network (DFN) models have been widely used to model heat extraction from EGSs (Moslehi et al. 2025). Pandey et al. (2015), Song et al. (2022b), Chen et al. (2018) and André et al. (2006) developed THC coupled models based on DFN to investigate fracture aperture evolution driven by water-rock reactions and the corresponding impact on heat extraction performance in EGSs. Their research found that undersaturated injection would induce dissolution reactions on fracture surfaces, leading to an increase in fracture aperture and a decrease in injection pressure. Conversely, for oversaturated injection, precipitation reactions occur and result in a decrease in fracture aperture and an increase in injection pressure.

However, most previous studies on HDR reservoirs only considered fracture reactive transport (FRT) and ignored the potential effect of matrix reactive transport (MRT) (André et al. 2006; Pandey et al. 2015; Chen et al. 2018; Song et al. 2022b). The underlying implicit hypothesis is that matrix permeability is significantly smaller than that of fractures, and MRT is unlikely to exert a remarkable effect on reservoir flow and heat transport processes. Our previous studies developed a THC model for karst geothermal reservoirs and considered the reactive transport in both matrix pores and fractures. The simulation results indicated that MRT actually significantly changed fracture deformation, thus affecting flow and heat transport in fractures (Ji et al. 2024). However, it remains unclear how MRT affects heat extraction performance in geothermal reservoirs with relatively low rock porosity/permeability, such as HDR reservoirs. The current study aims to systematically investigate the effect of MRT on fracture deformation and heat extraction performance in EGS reservoirs. We applied our previously developed pore-fracture dual-media thermal-hydraulic-chemical (THC) coupled model (Ji et al. 2024) to HDR reservoir simulations with updated geological and model parameters. Through a series of numerical simulations, we elucidate the underlying mechanisms by which MRT influences fracture deformation and heat extraction, and demonstrate that despite the low permeability of the rock matrix, MRT may still exhibit an inescapable effect on the heat extraction efficiency of EGS reservoirs. Furthermore, the effect of MRT on the thermal performance of fractured geothermal reservoirs, such as HDR, karst, and sandstone, is investigated. We have determined the critical thresholds for considering MRT in each type of fractured geothermal reservoir. The key findings provide valuable guidance for subsequent modelling: (i) the trade-off between accuracy and efficiency in geothermal production (MRT attenuates water-rock reactions within fractures, thereby influencing heat-extraction performance. For high-fidelity EGS simulations, MRT should be explicitly represented. If some loss of accuracy is acceptable in exchange for computational efficiency, the in-fracture reaction rate can be adjusted based on our results to balance accuracy and efficiency); and (ii) approaches for fracture-network inversion (when using tracers for fracture-network inversion, MRT offers a mechanistic explanation for late-time tailing in tracer breakthrough curves, thereby improving inversion accuracy and interpretability).

2. Numerical model

2.1. Model assumptions

This study focuses on the effects of reactive transport in matrix pores on the heat extraction performance of EGS. The following assumptions are made: (1) The reservoir is saturated with water. (2) In EGS operations, we typically use groundwater or river water as the heat-transfer fluid and therefore neglect salinity effects (Qureshi et al. 2022). Accordingly, the solutions in the reservoir are considered to be dilute solutions. (3) The temperature variations in solution caused by the endothermic and exothermic effects of water-rock reactions are neglected (Ji et al. 2023a, 2023b). (4) The mechanical effects on fractures/pores evolution and thermal performance are ignored (Ji et al. 2023a, 2023b). This is a limitation of this study, as it mainly focuses on reactive transport within the fractures and rock matrix. Therefore, we neglect mechanical coupling in this study. Future work will incorporate mechanical effects to further refine the model.

2.2. Governing equations

This study develops a dual pore-fracture medium model to investigate the influence mechanisms of reactive transport in matrix pores on the heat extraction performance of EGS. The physical processes occurring in each medium are governed by the following equations. The fluid flow within the reservoir is governed by the principle of mass conservation and Darcy's Law (Pruess, 2006; Cheng et al. 2016; Gao et al. 2024), represented as follows:

Porous rock matrix:

$$\frac{\partial\left(\varphi_{\mathrm{p}}\rho_{\mathrm{f}}\right)}{\partial t}-\nabla\cdot\left(\rho_{\mathrm{f}}u\right)=Q_{\mathrm{f}} \tag{1}$$

$$u=-\frac{k_{\mathrm{p}}}{\mu_{\mathrm{f}}}\left(\nabla p+\rho_{\mathrm{f}}g\nabla z\right) \tag{2}$$

Fracture:

$$d_{\mathrm{f}}\frac{\partial\left(\varphi_{\mathrm{f}}\rho_{\mathrm{f}}\right)}{\partial t}-\nabla\cdot\left(d_{\mathrm{f}}\rho_{\mathrm{f}}u\right)=d_{\mathrm{f}}Q_{\mathrm{f}}+Q_{1} \tag{3}$$

$$u=-\frac{k_{\mathrm{f}}}{\mu_{\mathrm{f}}}\left(\nabla p+\rho_{\mathrm{f}}g\nabla z\right) \tag{4}$$

Matrix-fracture interface:

$$Q_1 = \left(-\frac{\rho_f k}{\mu_f} \left(\nabla_n p - \rho_f g \nabla_n z \right) \right)_{\text{upper}} - \left(-\frac{\rho_f k}{\mu_f} \left(\nabla_n p - \rho_f g \nabla_n z \right) \right)_{\text{lower}} \tag{5}$$

where φ_p and φ_f denote the reservoir matrix porosity and fracture porosity, %, respectively. ρ_f represents the fluid density, kg/m^3. u denotes the flow velocity in the reservoir, m/s. The parameter Q_f is the mass source flow rate, kg/(m^3·s). μ_f indicates the fluid dynamic viscosity, Pa·s. p is the fluid pressure, Pa. The item $\rho_f g \nabla z$ represents the effect of gravity. Q_1 is the mass flux between rock matrix pores and fractures, kg/(m^3·s). The terms "upper" and "lower" represent the upper and lower surfaces of the fracture, respectively. k_p and k_f correspond to the pore and fracture permeability, m^2. d_f expresses the fracture aperture, m. Note that fracture conductivity can be expressed by the cubic law, which will be introduced in subsequent sections.

In this study, the local thermal equilibrium model is adopted to govern heat transfer in the reservoir (Shi et al. 2023; Yang et al. 2023). The energy conservation equation is expressed as:

Porous rock matrix:

$$(\rho C_p)_{\text{eff}} \frac{\partial T}{\partial t} + \rho_f C_{p,f} u \cdot \nabla T - \nabla \cdot \left(\lambda_{\text{eff}} \nabla T \right) = Q_E \tag{6}$$

Fracture:

$$d_f (\rho C_p)_{\text{eff}} \frac{\partial T}{\partial t} + d_f \rho_f C_{p,f} u \nabla (T) - \nabla \cdot \left(d_f \lambda_{\text{eff}} \nabla T \right) = d_f Q_E + Q_2 \tag{7}$$

Matrix-fracture interface:

$$Q_2 = \left(\rho_f C_{p,f} (u \cdot n) T - \lambda_{\text{eff}} \nabla_n T \right)_{\text{upper}} - \left(\rho_f C_{p,f} (u \cdot n) T - \lambda_{\text{eff}} \nabla_n T \right)_{\text{lower}} \tag{8}$$

where T represents the fluid temperature, K. Q_E is an external heat source, W/m^3. Q_2 indicates the heat fluxes between the matrix and fractures, W/m^3. It is defined as the difference in normal heat fluxes from the matrix at the top and bottom surfaces of the fracture. C_p denotes the heat capacity, J/(kg·°C). $(\rho C_p)_{\text{eff}}$ and λ_{eff} represent the effective volumetric heat capacity and the effective thermal conductivity respectively, expressed as:

$$(\rho C_p)_{\text{eff}} = (1 - \varphi) \rho_s C_{p,s} + \varphi \rho_f C_{p,f} \tag{9}$$

$$\lambda_{\text{eff}} = (1 - \varphi) \lambda_s + \varphi \lambda_f \tag{10}$$

where ρ_s, $C_{p,s}$, and λ_s indicate the density, heat capacity and thermal conductivity of the reservoir solid component, kg/m^3, J/(kg·°C) and W/(m·°C), respectively. $C_{p,f}$ and λ_f are the heat capacity and thermal conductivity of the fluid in the reservoir, J/(kg·°C) and W/(m·°C), respectively.

The variations in temperature and solute concentration caused by fluid circulation further disrupt the reservoir's chemical equilibrium, leading to mineral dissolution and precipitation, which modify pore and fracture structures. Building on the previous model, we explicitly consider water-rock reactions in both the rock matrix and fractures, as well as the mass transfer processes between them. The mass transfer and reaction processes are modeled using transport and reaction kinetic equations. The solute transport process in the reservoir involves both convection and diffusion, and the corresponding solute transport equation is given as follows:

Porous rock matrix:

$$\frac{\partial \left(\varphi_p \rho_f c_{i,p} \right)}{\partial t} - D_i \nabla \left(\rho_f c_{i,p} \right) + u \cdot \nabla \left(\rho_f c_{i,p} \right) = \varphi_p R_i{}^p \tag{11}$$

Fracture:

$$d_f \left[\frac{\partial \left(\rho_f c_{i,f} \right)}{\partial t} - D_i \nabla \left(\rho_f c_{i,f} \right) + u \cdot \nabla \left(\rho_f c_{i,f} \right) \right] = d_f R_i{}^f + Q_3 \tag{12}$$

Matrix-fracture interface:

$$Q_3 = \left(\rho_f c_{i,p} - D_i \frac{\partial \left(\rho_f c_{i,p} \right)}{\partial z} \right)_{\text{upper}} - \left(\rho_f c_{i,p} - D_i \frac{\partial \left(\rho_f c_{i,p} \right)}{\partial z} \right)_{\text{lower}} \tag{13}$$

$$c_{i,p}\big|_{\text{upper}} = c_{i,p}\big|_{\text{lower}} = c_{i,f} \tag{14}$$

where D_i indicates the effective diffusion coefficient of substance "i" in solution, m^2/s. $c_{i,p}$ and $c_{i,f}$ denote the concentration of substance "i" within pores and fractures, mol/m^3. R_i^p and R_i^f correspond to the reaction rate in matrix pores and fractures, mol/(m^3·s), respectively. Q_3 represents the exchange fluxes between matrix pores and fractures, mol/(m^2·s).

Hot dry rocks are predominantly composed of granite, with water-rock reactions primarily involving the dissolution and precipitation of quartz (Ji et al. 2025). The primary objective of this study is to explore the competition mechanisms between reactive transport in matrix pores and that in fractures, as well as their corresponding influence on the heat-extraction performance of EGS. Therefore, we consider only the principal reactive mineral (quartz) to clarify the core mechanisms of interest. Neglecting the water-rock reactions of other minerals in granite, compared with our earlier research (Ji et al. 2025), results in a 28.6% underestimation of the overall reaction rate and a 16.5% reduction in fracture aperture evolution. Notably, for other reservoir types, users can introduce feldspar, mica or even clay reactions by simply adding extra source terms in the same PDE weak form Eqs. (15)–(18). The chemical reaction formula is expressed as:

$$SiO_2(s) + 2H_2O(l) \Leftrightarrow H_4SiO_4(aq) \tag{15}$$

The chemical reaction is controlled by kinetics, and the reaction rate for quartz ($R_{(SiO_2)}$) is expressed as (André et al. 2006):

$$R_{(SiO_2)} = A_{(SiO_2)} k^+_{(SiO_2)} \mho_{(SiO_2)} \quad \mho_{(i)} = 1 - \frac{c_{(SiO_2)}}{c_{eq(SiO_2)}} \tag{16}$$

$$k^+_{(SiO_2)} = k^+_{(SiO_2),25\,°C} \times \exp\left[\frac{-E_a}{R} \times \left(\frac{1}{T} - \frac{1}{298.15} \right) \right] \tag{17}$$

$$\log\left(c_{eq(SiO_2)} \right) = -43.084 - 0.00594T + \frac{1539.697}{T} + 16.52 \times \log(T) - \frac{189816.23}{T^2} \tag{18}$$

where $A_{(SiO_2)}$ is the specific surface area of quartz (Ji et al. 2023b), 1/m. It refers to the total area per unit mass of minerals involved in the reaction, which means the area of minerals contacted per unit volume of H_2O under the background of this study (Xu et al. 2007). $k^+_{(SiO_2)}$ denotes the reaction rate constant of quartz, mol/(m^2·s). $\mho_{(SiO_2)}$ indicates the degree of unsaturation, which represents the deviation of the solution concentration from its equilibrium state. When the $\mho_{(SiO_2)}$ is greater than zero, the solution is undersaturated, leading to a dissolution reaction. Conversely, the solution is in an oversaturated state, leading to a precipitation reaction. Additionally, a larger absolute value of $\mho_{(SiO_2)}$ corresponds to a faster reaction rate. $k^{+}_{(SiO_2),25\ ^{\circ}C}$ is the reaction rate constant of quartz at ambient temperature, mol/(m^2·s). E_a and R represent reaction activation energy and the molar gas constant, kJ/mol and J/(mol·K), respectively. $c_{eq(SiO_2)}$ is the equilibrium concentration of quartz, mol/m^3.

Pores and fractures undergo deformation due to water-rock interactions, and the relationship between deformation and reaction rate is presented below (Pandey et al. 2015):

$$\frac{\partial \varphi_p}{\partial t} = \frac{\varphi_p R_{SiO_2} M_{SiO_2}}{\rho_{SiO_2}} \quad \frac{\partial d_f}{\partial t} = \frac{d_f R_{SiO_2} M_{SiO_2}}{\rho_{SiO_2}} \tag{19}$$

where M_{SiO_2}, and ρ_{SiO_2} denote the molar masses and density of quartz, kg/mol and kg/m^3, respectively. Since permeability and specific surface area are related to porosity and fracture aperture, the corresponding expressions are provided below (Song et al. 2022b):

$$k_p = k_0 \left(\frac{\varphi_p}{\varphi_0}\right)^3 \left(\frac{1-\varphi_0}{1-\varphi_p}\right)^2 \quad k_f = \frac{{d_h}^2}{12} \tag{20}$$

$$d_h = d_{h0} + f_f\left(d_f - d_{f0}\right) \tag{21}$$

$$A_{(SiO_2)} = A_0 \frac{\varphi_p}{\varphi_0} \frac{\log(\varphi_p)}{\log(\varphi_0)} \tag{22}$$

where k_0 and φ_0 denote the initial permeability and porosity of the rock matrix pores, m^2 and %, respectively. d_h and d_{h0} represent the hydraulic aperture and the initial fracture hydraulic aperture of fractures, mm, respectively. d_f and d_{f0} are the fracture aperture and the initial fracture aperture, mm, respectively. f_f reflects the coefficient that describes the transformation between the two types of apertures (Witherspoon et al. 1979). A_0 is the initial specific surface area of quartz, 1/m.

To effectively assess the system's thermal performance, parameters such as production temperature T_{out}, °C; power generation *We*, MW; pressure difference between the injection and production well Δp, MPa; and hydraulic conductivity K ($K = k\rho_f g/\mu_f$, m/s) are introduced to represent the thermal performance of the geothermal reservoir. The calculation equations for each thermal performance index can be found in our previous studies (Song et al. 2021; Ji et al. 2024; Xu et al. 2024).

3. Model setting

3.1. A field-scale matrix-fracture EGS model

To model the thermal-hydraulic-chemical coupled processes in EGS reservoirs, we develop a 3D field-scale EGS model based on the Gonghe EGS site (Lei et al. 2020), including a discrete fracture network region and the surrounding rock domain, as shown in Fig. 1. The model is sufficiently large to minimize boundary effects on subsequent numerical simulations (Song et al. 2018), with a dimension of 1000 m × 1000 m × 1000 m, and its top is located 3300 m below the ground surface. At the center of the model, we set a 500 m cube to represent the stimulated reservoir volume (SRV), which encompasses hydraulic and natural fractures, rock matrix adjacent to the fractures, and injection/production wells. Since fractures in HDRs are generally densely distributed and the precise delineation of fracture distribution is extremely difficult,

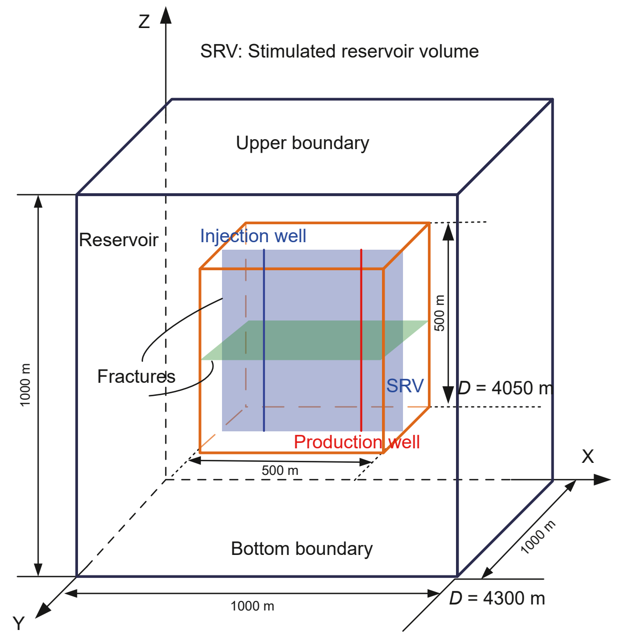

Fig. 1. The schematic representation of the field-scale matrix-fracture EGS model (including surrounding rock, SRV, fractures, injection and production wells).

we simplify the SRV as a porous medium with a relatively higher permeability compared with the intact rock formations outside the SRV. Such an equivalent porous media method has been widely used in subsurface reservoir modeling (Pandey et al. 2015; Chen et al. 2018; Song et al. 2022b). We also assume a vertical and a horizontal fracture to connect the injection and production wells (Pandey et al. 2015; Chen et al. 2018; Song et al. 2022b). The two fractures are 500 m ×500 m in size and are located at the center of the SRV (Fig. 1). The diameters of the injection and production wells are 0.1 m, and the distance between them is 400 m. The open-hole section of the two wells extends across the vertical fracture with a length of 500 m. Table 1 summarizes the parameters defined for the reservoir, SRV, the two fractures, and the injection/production wells. We use COMSOL Multiphysics, a

Table 1
The physical properties of the reservoir (Blanc et al. 2012; Wang et al. 2020; Lv et al. 2022).

Items	Values
Density of the reservoir, kg/m^3	2800
Heat conductivity of the reservoir, W/(m·K)	3
Heat capacity of the reservoir, J/(kg·K)	1000
Porosity of the reservoir, %	1
Permeability of the reservoir, mD	1×10^{-3}
Density of the SRV, kg/m^3	2600
Heat conductivity of the SRV, W/(m·K)	2.51
Heat capacity of the SRV, J/(kg·K)	754.4
Porosity of the SRV, %	5
Permeability of the SRV, mD	0.5
Density of the fracture, kg/m^3	2000
Heat conductivity of the fracture, W/(m·K)	2.5
Heat capacity of the fracture, J/(kg·K)	750
Porosity of the fracture, %	100
Initial fracture aperture, mm	1
Hydraulic aperture d_{h0}, m	2.45×10^{-5}
Coefficient of fracture irregularity f_f	1
Initial specific surface area of pores A_0, 1/m	8000
Wellbore diameter, m	0.1
Diffusion coefficient D, m^2/s	1×10^{-9}
Molar mass of quartz, g/mol	60

widely used multiphysical coupled numerical simulation platform, to model the THC processes in the developed model.

3.2. Initial and boundary conditions

The initial temperature and pressure increase linearly from the top boundary to the bottom boundary, with gradients of 0.07 °C/m and 8 kPa/m for temperature and pressure, respectively. The initial concentration of SiO_2 is 3.41 mol/m^3 and satisfies chemical equilibrium. At the top boundary, the temperature is 138 °C and the pressure is 33 MPa. The top and bottom boundaries are considered thermally insulated, and the side boundaries are maintained at the initial temperature. The injection flow rate is 30 kg/s with an injection temperature of 60 °C. The pressure at the bottom of the production well is maintained at 30 MPa. Note that the concentration of SiO_2 in the injection fluid is 0 mol/m^3, indicating an undersaturated injection condition. Water-rock reactions occur within both the fractures and matrix pores, with mass exchange occurring between them. The simulation runs for 30 years and the initial and boundary condition parameters are listed in Table 2.

3.3. Simulation mesh and model validation

The geometric and physical models in this study are similar to those used in our previous study (Ji et al. 2024), thus the same meshing method is applied. The mesh in the SRV is refined because this region is the primary area for fluid flow, heat transfer, and chemical reactions. A free triangular mesh is adopted to divide the upper boundary of this region, which is then swept from the upper to the bottom boundary, resulting in 289,760 elements. The rest of the reservoir (surrounding rock) is divided by a free tetrahedral mesh (Fig. 2). The final mesh number is 385,405. A mesh-independence analysis was performed in our previous study (Ji et al. 2024), and therefore not repeated here.

Given the absence of experimental and field data, an accurate analytical solution serves as a viable and reliable method for model validation. Owing to the complexity of the THC coupling mechanism, the THC coupled model is broken down into TH and HC sub-models for individual validation. The TH coupled model is validated by an analytical solution for fluid flow and heat transfer in a 2D infinite rock matrix with a single fracture (Song et al. 2018; Ji et al. 2022), which is expressed by:

$$T_\mathrm{f} = T_\mathrm{r} + (T_\mathrm{in} - T_\mathrm{r})\,erfc\left(\frac{\lambda_\mathrm{r} x \Big/ \left(\rho_\mathrm{f} c_\mathrm{p,f} d_\mathrm{f}\right)}{\sqrt{u_\mathrm{in}(u_\mathrm{in} t - x)\lambda_\mathrm{r} \big/ \left(\rho_\mathrm{s} c_\mathrm{p,s}\right)}}\right) U\left(t - \frac{x}{u_\mathrm{in}}\right) \tag{23}$$

where T_f represents the fracture temperature, K; *erfc* denotes the complementary error function and U represents the unit step function. The subscripts “s” and “f” indicate the rock matrix and water, respectively. The HC coupled model is validated by an analytical model for solute transport in a prescribed groundwater flow field (Wilson and Miller, 1978), which is given as follows:

$$c_\mathrm{ana} = \frac{M \times e^{\frac{\left\{-[(x-x_0)-ut]^2 \times \left(2tD_{yy}+d^2\right) - [(y-y_0)-vt]^2 \times \left(2tD_{xx}+d^2\right) + [(x-x_0)-ut] \times [(y-y_0)-vt]4tD_{xy}\right\}}{\left[8t^2\left(D_{xx}D_{yy}-{D_{xy}}^2\right)+2d^4+4d^2t\left(D_{xx}+D_{yy}\right)\right]}}}{2\pi n_\mathrm{e}\sqrt{4t^2\left(D_{xx} \times D_{yy} - {D_{xy}}^2\right) + d^4 + 2d^2t(D_{xx}+D_{yy})}} \tag{24}$$

where M denotes the solute source, mol/m^3. x_0 and y_0 represent the coordinates of the solute source (−200, 200), m. D_{xx}, D_{yy}, and D_{xy} denote the dispersion tensor *xx*, *yy*, and *xy* components, m^2/s, respectively. d is the width of the injection area, m. n_e is the effective porosity. u and v indicate the horizontal and vertical velocity, m/s. Fig. 3 presents a comparison of the results derived from the numerical and analytical solutions of the TH and HC coupled models. The specific validation process is also detailed in our previous study (Ji et al. 2024).

Notably, this validation is limited because the TH and HC processes are validated separately. A further validation of the fully coupled THC model is necessary yet challenging due to the lack of analytical solutions and well constrained experiments. In future work, we will employ two complementary experimental approaches to further validate our model. The first involves core-scale THMC coupled-process experiments designed to observe variations in the hydraulic aperture of fractures within rock cores under varying conditions, including temperature, pore pressure, confining pressure, and injected-solution composition. The second consists of microfluidic chamber experiments at the micro- and nanoscale to characterize reactive transport between fractures and the surrounding matrix, thereby providing direct insight into the interaction mechanisms that govern fracture-matrix reactive transport.

Table 2
Initial and boundary conditions parameters for the base case (Wilson and Miller, 1978; Wang et al. 2020).

Items	Values
Injection temperature, °C	60
Injection rate, kg/s	30
Production pressure, MPa	33
Temperature gradient, °C/m	0.07
Pressure gradient, Pa/m	8000
Temperature at the top of the boundary, °C	138
Pressure at the top of the boundary, MPa	33
Initial concentration of SiO_2, mol/m^3	3.41
Injection concentration of SiO_2, mol/m^3	0

4. Results and discussions

4.1. Analysis of thermal performance

As aforementioned, this study primarily aims to investigate the effect of reactive transport in the matrix on the heat extraction performance of EGS and to elucidate the influence mechanisms of MRT. We conduct two simulations: one includes reactive transport in both matrix pores and fractures (MFRT), and the other only considers reactive transport in fractures (FRT). We compare the simulation results by analyzing pressure, fracture aperture, temperature, and concentration distributions qualitatively, as well as geothermal productivity indices quantitatively, aiming to comprehensively understand how reactive transport in matrix pores affects the thermal performance of EGS. The comparison of

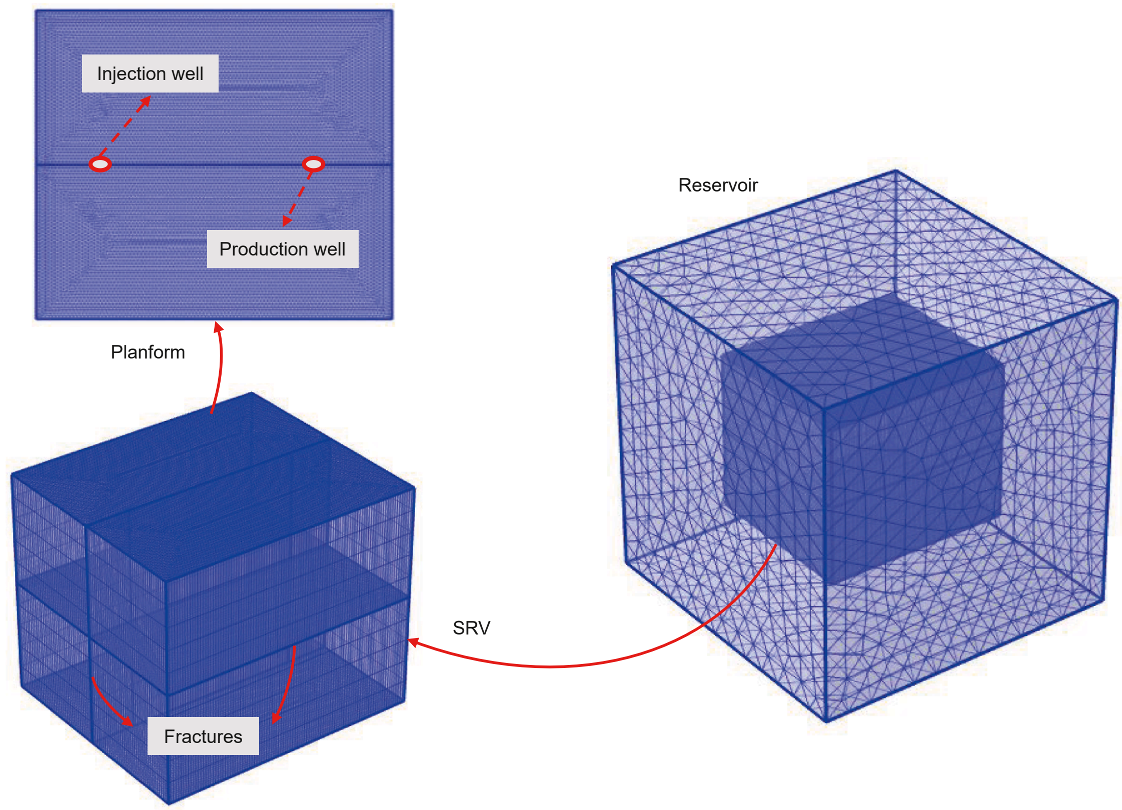

Fig. 2. Numerical meshing schemes (the upper boundary of SRV is divided by a free triangular mesh and swept from the upper boundary to the bottom boundary to divide the SRV; the surrounding rock is divided by a free tetrahedral mesh).

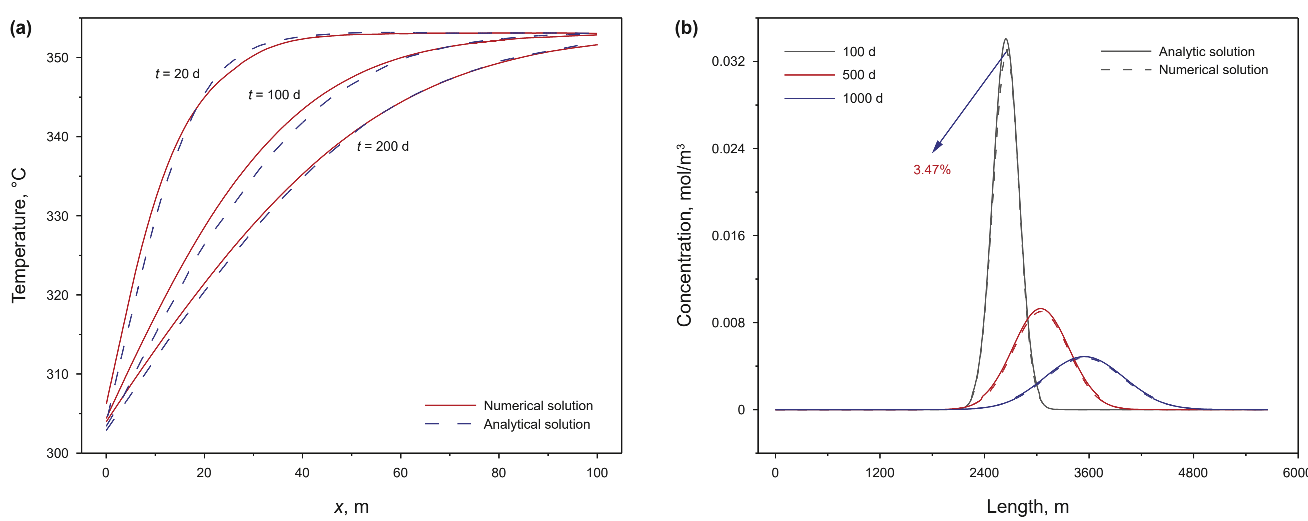

Fig. 3. **(a)** Temperature distribution along the fracture at different times in the TH coupled model. **(b)** Comparison of concentrations between analytical and numerical solutions along the diagonal line in the HC coupled model.

pressure indicates that the injection pressure in the MFRT case is significantly higher than that in the FRT case (Fig. 4(a)), and the pressure disparity between the two simulations becomes increasingly evident as extraction progresses. The fracture aperture in the MFRT case remains nearly constant, while the FRT case shows a considerable aperture increase especially in the horizontal fracture (Fig. 4(b)). Such a difference between the two cases indicates that reactive transport in matrix pores retards fracture aperture evolution. The reduction in fracture aperture change can enhance reservoir integrity and reduce the risk of fluid leakage, thereby helping maintain system integrity (Aminnaji et al. 2024).

In the MFRT case, the low-concentration region spreads uniformly from the injection well to the production well. Conversely, in the FRT case, the low-concentration region swiftly reaches the production well in the first year (Fig. 4(d)). This is because fractures serve as major flow channels in HDRs, and the increase in

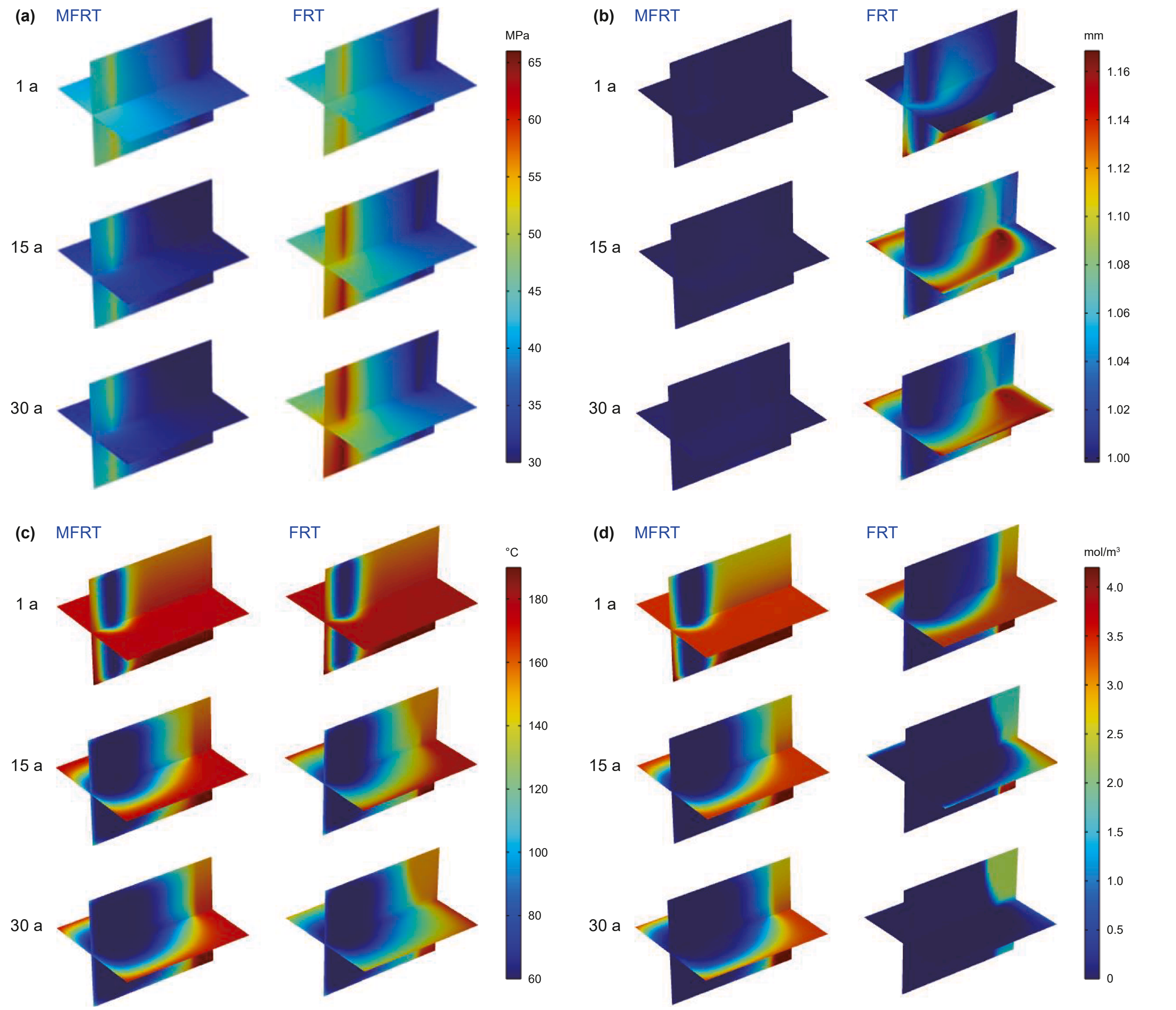

Fig. 4. Comparison of **(a)** pressure, **(b)** fracture aperture, **(c)** temperature, and **(d)** concentration between the MFRT case (the left side of each image) and the FRT case (the right side of each image) at different times (1 a, 15 a, and 30 a).

fracture aperture is greater in the FRT case (Fig. 4(b)). Therefore, neglecting the influence of MRT enables the injected low-concentration fluid to propagate swiftly along the fracture surfaces and reach the production wells more quickly. This further confirms that there is a mutual competition between MRT and FRT, which can alter the concentration distribution within the reservoir and subsequently affect the evolution of fracture aperture (Ji et al. 2024).

The qualitative analysis of physical field distributions reveals that MRT can influence the concentration distribution within the reservoir, which subsequently affects the fracture aperture evolution and the evolution of the temperature and flow fields within the reservoir. To further quantitatively investigate the effect of MRT on thermal performance of EGS, we compare the thermal indices of the MFRT and FRT cases. The rate of production temperature decay in the MFRT case is lower than that in the FRT case. Over 30 years of production, the initial production temperature of 173 °C gradually decreases to 152.53 °C (MFRT) and 142.35 °C (FRT), respectively. Thermal breakthrough is defined as a 10% drop in the initial production temperature (Song et al. 2021), that is, when the production temperature reduces to 155.7 °C, marking the occurrence of thermal breakthrough. Neglecting the MRT leads to an underestimation of the thermal breakthrough time (Fig. 5(a)). Thermal breakthrough occurs at 24.5 years after fluid injection starts in the MFRT case, while it decreases to 7.5 years in the FRT case. This is because the MRT slows down fracture surface deformation and weaken the preferential flow effects along the fractures. As a result, the temperature distribution would be more uniform towards the production well (Fig. 4(c)). In the MFRT case, the pressure difference between the injection and production wells increases from the initial value of 19.37 MPa–33.78 MPa over 30 years of production. In contrast, in the FRT case, the pressure difference exhibits a rapid increase followed by a decrease in the first 10 years, and then gradually increases afterward (Fig. 5(b)). Neglecting the MRT results in a 45.94% underestimation of the pressure difference. This conclusion aligns with previous research findings on karst geothermal reservoirs (Ji et al. 2024).

Similar to the temperature variation in Fig. 5(a), power generation decreases from 1.97 MW (initial stage) to 1.34 MW (MFRT) and 1.07 MW (FRT), as shown in Fig. 5(c). If the MRT is neglected,

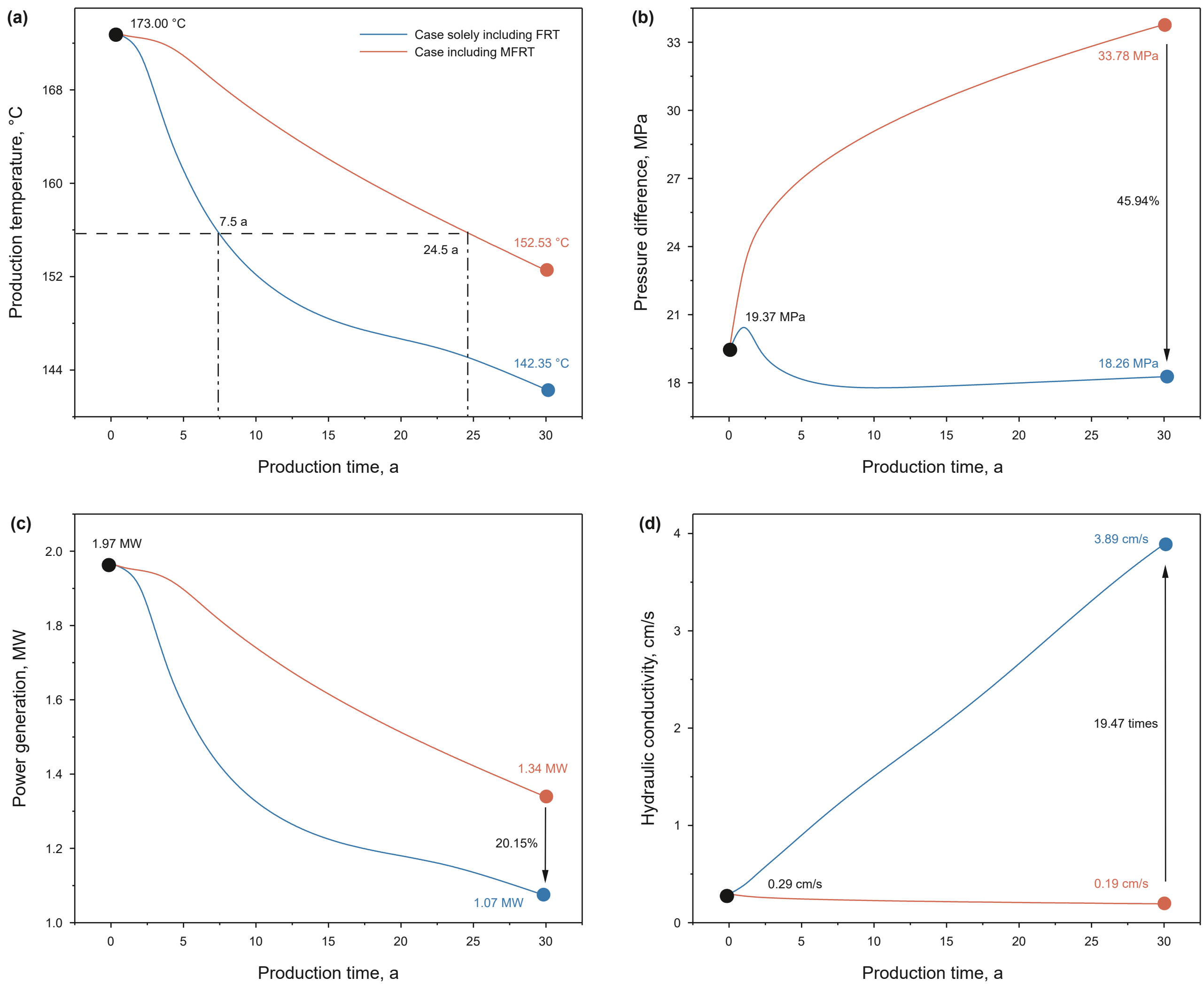

Fig. 5. Comparison of **(a)** production temperature, **(b)** injection-production pressure difference, **(c)** power generation, and **(d)** hydraulic conductivity between MFRT and FRT cases.

power generation would be underestimated by 20.15% over 30 years of production. This is because the MRT mitigates thermal breakthroughs, thereby increasing power generation. The hydraulic conductivity of the SRV between the injection and production wells exhibits opposite trends in the two cases (Fig. 5(d)). In the MFRT case, the hydraulic conductivity decreases from 0.29 to 0.19 cm/s. Conversely, in the FRT case, it increases from 0.29 to 3.89 cm/s. The above analysis indicates that the MRT has a significant effect on fracture flow and reservoir thermal performance during the exploitation of HDRs.

4.2. Influence mechanisms of MRT on EGS heat extraction

The analysis above highlights that the MRT significantly influences EGS heat extraction. This section aims to further explore the underlying mechanisms and understand how MRT affects fracture flow and heat transport processes. Based on the above analysis, we posit that the MRT affects the reservoir's concentration distribution, thereby influencing the reaction and deformation rates at the fracture surface. To confirm this hypothesis, we compare the degree of unsaturation in the fractures and the reaction rate at the fracture surface across the two different cases (Fig. 6). The distribution of the degree of unsaturation is closely associated with the concentration distributions. In the MFRT case, the high-unsaturation region spreads evenly from the injection well to the production well as low-concentration fluids are injected (Fig. 6(a)). Meanwhile, these distribution characteristics closely resemble those of the temperature distribution (Fig. 4(c)). By contrast, in the FRT case, the high-unsaturation region rapidly reaches the production well within the first year (Fig. 6(a)).

The reaction rate at the fracture surfaces in the MFRT case is significantly smaller than that in the FRT case (Fig. 6(b)). This is because the reaction rate, controlled by both the reaction rate constant (which increases with temperature) and the degree of unsaturation, is positively correlated with both factors (Eq. (16)). In the FRT case, the velocity of solute transport within the fractures is higher than the velocity of temperature diffusion. Consequently, higher reaction rates occur at the forefront of the low-temperature spread area (Fig. 6(b)). This observation is in accordance with previous research findings (Ji et al. 2025). However, in the MFRT case, the reaction rates on the fracture surfaces are comparatively low. This is because the high-unsaturated regions coincide with low-temperature areas (associated with a low reaction rate constant), and the low-unsaturated regions (Fig. 6(a)) correspond to high-temperature zones (Fig. 4(c)). This indicates that the MRT affects the degree of unsaturation in fractures by altering the solute transfer process at the fracture surfaces, thus influencing both fracture reactions and deformation (Ji et al. 2024).

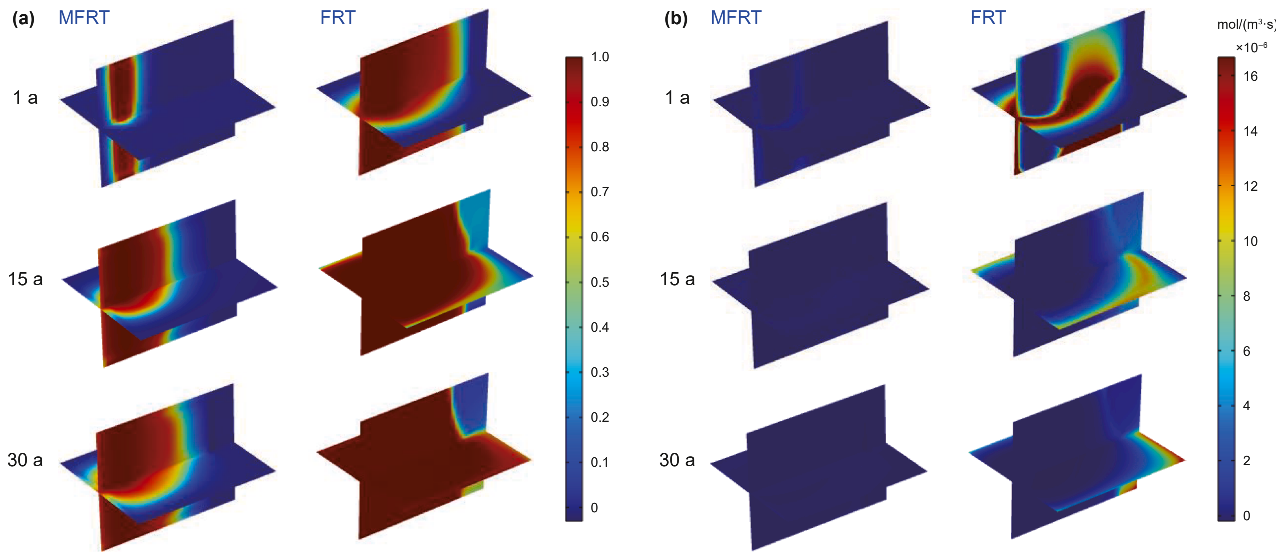

Fig. 6. Comparison of **(a)** degree of unsaturation in fracture and **(b)** reaction rate at fracture surface between MFRT and FRT cases at different times.

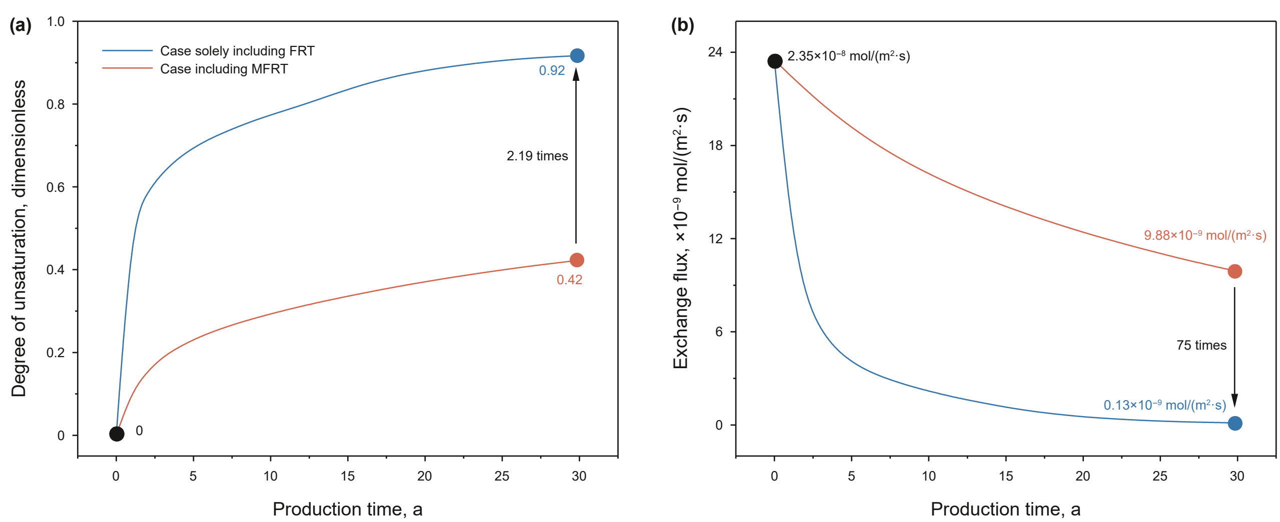

Fig. 7. Comparison of the variation in **(a)** degree of unsaturation in fractures, and **(b)** exchange fluxes between matrix pores and fractures between MFRT and FRT case.

To further validate the above statement, we quantitatively compare the average degree of unsaturation on the fracture surfaces over time. In the FRT case, the degree of unsaturation reaches a high level in the initial production stage (Fig. 7(a)). During the injection of low saturation water in 30 years, the degree of unsaturation in fractures increases from zero (initial) to 0.42 and 0.92 for the two cases, respectively. The results of this quantitative analysis further corroborate the aforementioned hypothesis that the MRT can alter the solute concentration distribution at the fracture surfaces, thereby affecting their reaction and deformation rates. According to Eqs. (11)–(14), the interaction between the matrix and the fractures is reflected in the solute exchange fluxes between them. This suggests that the MRT likely enhances the exchange fluxes between matrix pores and fractures. Fig. 7(d) strongly supports this explanation: the solute exchange fluxes between matrix pores and fractures in the MFRT case is 75 times higher than that in the FRT case. This indicates that the MRT can enhance the exchange fluxes between matrix pores and fractures, thereby affecting the solute concentration distribution at the fracture surfaces.

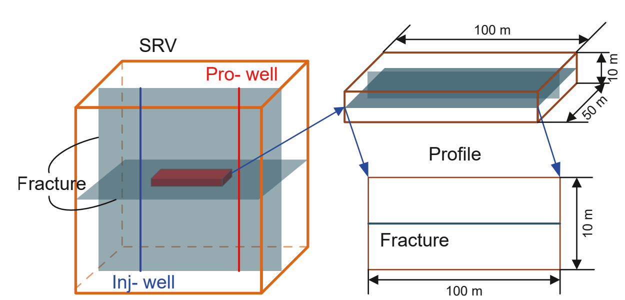

Fig. 8. Intercepting the area (100 m × 50 m × 10 m) near the fracture for local observation. (Inj-well: injection well; Pro-well: production well. The profile is positioned on the front surface of the rectangular prism.)

We extracted a 100 m × 50 m × 10 m rectangular prism from the central region of the intersection of fractures (Fig. 8) to visually compare the solute mass transfer process between the fracture surfaces and matrix pores under the two cases. The concentration

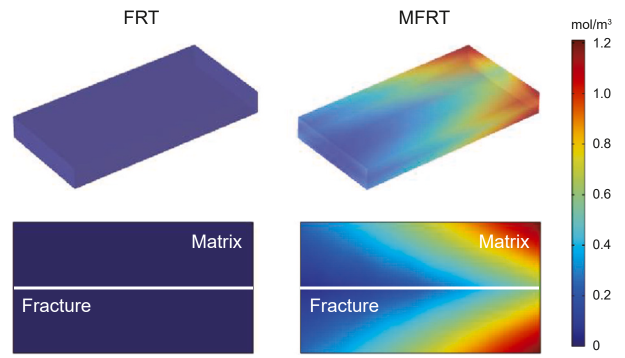

Fig. 9. Concentration distribution in the matrix near the fracture and fracture over 15 years of production. The top row features a 3D concentration distribution, while the bottom row presents a vertical profiles.

distribution along the vertical profiles of the prism is presented for the two cases (Fig. 9). The concentration in the fractures and the adjacent matrix remain nearly identical in the FRT case. This indicates that the mass transfer between the fractures and the surrounding matrix pores would be minimal when solely considering the FRT. On the contrary, the concentration in the matrix adjacent to the fractures is significantly higher than that within the fractures in the MFRT case. This indicates that solutes from the matrix pores are transported into the fractures. This small-scale observational analysis (Cai et al. 2025) further substantiates the above conclusions, which suggest that the MRT can enhance the exchange fluxes from matrix pores to fractures, thereby influencing the solute concentration distribution at the fracture surfaces. The phenomena observed in Ling et al.'s microfluidic experiments on reactive transport in fractures (Ling et al. 2022) provide some support for our interpretation.

4.3. Analysis of exchange fluxes between fracture and matrix pores

Based on the above analysis, the MRT enhances the exchange fluxes between fractures and matrix pores, thereby influencing the solute concentration distribution at the fracture surfaces, affecting fracture deformation, and ultimately impacting the system's heat extraction performance. According to Eqs. (13) and (14), the exchange fluxes between fractures and matrix pores is determined by the diffusion coefficient and the concentration gradient between fractures and matrix pores. The concentration gradient is affected by the reaction rate (driven by temperature and concentration), the mass transfer rate (determined by fluid flow and reservoir porosity/permeability characteristics), and the initial concentration difference. Therefore, this section explores the effects of the diffusion coefficient, reaction rate constant, matrix porosity and permeability, and the initial concentration on the exchange fluxes between fracture and matrix pores, aiming to identify the key factors governing the exchange fluxes. To examine the influence of the aforementioned parameters, additional simulations are conducted by varying each parameter individually (Table 3). The reaction rate constants are based on reactions at 150 °C and cover the order of magnitude of common mineral reaction rate constants in geothermal reservoirs (Xu et al. 2004, 2007; Holmslykke et al. 2017). Similarly, the porosity and permeability values used are representative of typical geothermal reservoirs (Xu et al. 2004, 2007). In these cases, a porosity of 5% and permeability of 0.5 mD correspond to hot dry rock, a low-permeability reservoir. A porosity of 10% and permeability of 10 mD are representative of karst (Ji et al. 2024), a medium-permeability reservoir. Meanwhile, a porosity of 20% and permeability of 50 mD align with sandstone, indicative of a high-permeability reservoir. The initial concentrations are set at different saturation states: 0 c_{eq}, 0.5 c_{eq}, c_{eq}. Bold text indicates the base case.

Table 3
Parameter settings for different influencing factors (Xu et al. 2004, 2007; Holmslykke et al. 2017; Ji et al. 2024).

Influencing factors	Values
Diffusion coefficient, m^2/s	1×10^{-11}, $\mathbf{1\times10^{-9}}$, 1×10^{-7}
Reaction rate constant, mol/(m^2·s)	2.4×10^{-11}, $\mathbf{2.4\times10^{-9}}$, 2.4×10^{-7}
Matrix porosity and permeability, % and mD	**5, 0.5**; 10, 10; 20, 50
Initial concentration, mol/m^3	0, 0.5 c_{eq}, $\mathbf{c_{eq}}$

Fig. 10 provides a visual comparison of how various factors affect the exchange fluxes between fractures and matrix pores. This is a deterministic parameter-combination simulation that does not include any stochastic variability. The exchange fluxes in the MFRT case is significantly greater than that in the FRT case (Fig. 10). Meanwhile, these influencing factors affect the exchange fluxes to varying degrees. The exchange fluxes increases with the diffusion coefficient, but the variation is minimal (Fig. 10(a)). Given that the diffusion coefficient represents molecular diffusion intensity, it is plausible to conclude that the exchange fluxes between matrix pores and fractures may be convection-dominated. This hypothesis will be thoroughly analyzed in the subsequent section. Reaction rate constants exert different influences on the exchange fluxes in the MFRT case and the FRT case. In the MFRT case, the exchange fluxes initially increases and then decreases with the reaction rate constants, peaking at a reaction rate constant of 2.4×10^{-9} mol/(m^2·s). In the FRT case, the exchange fluxes increases with the reaction rate constants, and it increases dramatically as the reaction rate constant increases from 2.4×10^{-9} to 2.4×10^{-7} mol/(m^2·s) (Fig. 10(b)). This is attributed to the diverse time scales of reaction and mass transfer rates, which are in a complex competition with each other (Song et al. 2022b; Ji et al. 2025). This phenomenon will be discussed in detail in connection with Figs. 13(a) and 14. The exchange fluxes rapidly increase with increasing matrix porosity and permeability, indicating they are key factors affecting the exchange fluxes. This conclusion aligns with the phenomena observed in previous experiments on micro-scale fracture reaction transport (Ling et al. 2022). The exchange fluxes increases with the initial concentration, as the concentration gradient between the matrix and fractures grows with it. However, solute exchange between the matrix and fractures is advectively dominated (Fig. 11). Therefore, the variation is minimal, indicating that the effect of the initial concentration difference on the exchange fluxes is quickly overtaken by mass transfer and reaction processes.

Based on the diffusion coefficient analysis, exchange fluxes between matrix pores and fractures may be primarily driven by convection. The Peclet number (the ratio of convection rate to diffusion rate) (Blanc et al. 2012) is adopted in this study to quantitatively evaluate the relative strength of convection and diffusion for validating this conclusion. The Peclet number is given by $Pe = uL/D_e$, where u denotes the mean velocity, m/s; L is the characteristic length, m; and D_e is the effective diffusion coefficient, m^2/s. The Pe in the matrix increases with matrix porosity/permeability, while that at the matrix-fracture interface falls with higher matrix porosity/permeability. This is because enhanced matrix porosity/permeability boost the mass transfer rate within the matrix (Fig. 11). However, under all these matrix porosity/permeability conditions, the Peclet number in the matrix is less than one, while that at the matrix-fracture interface exceeds one.

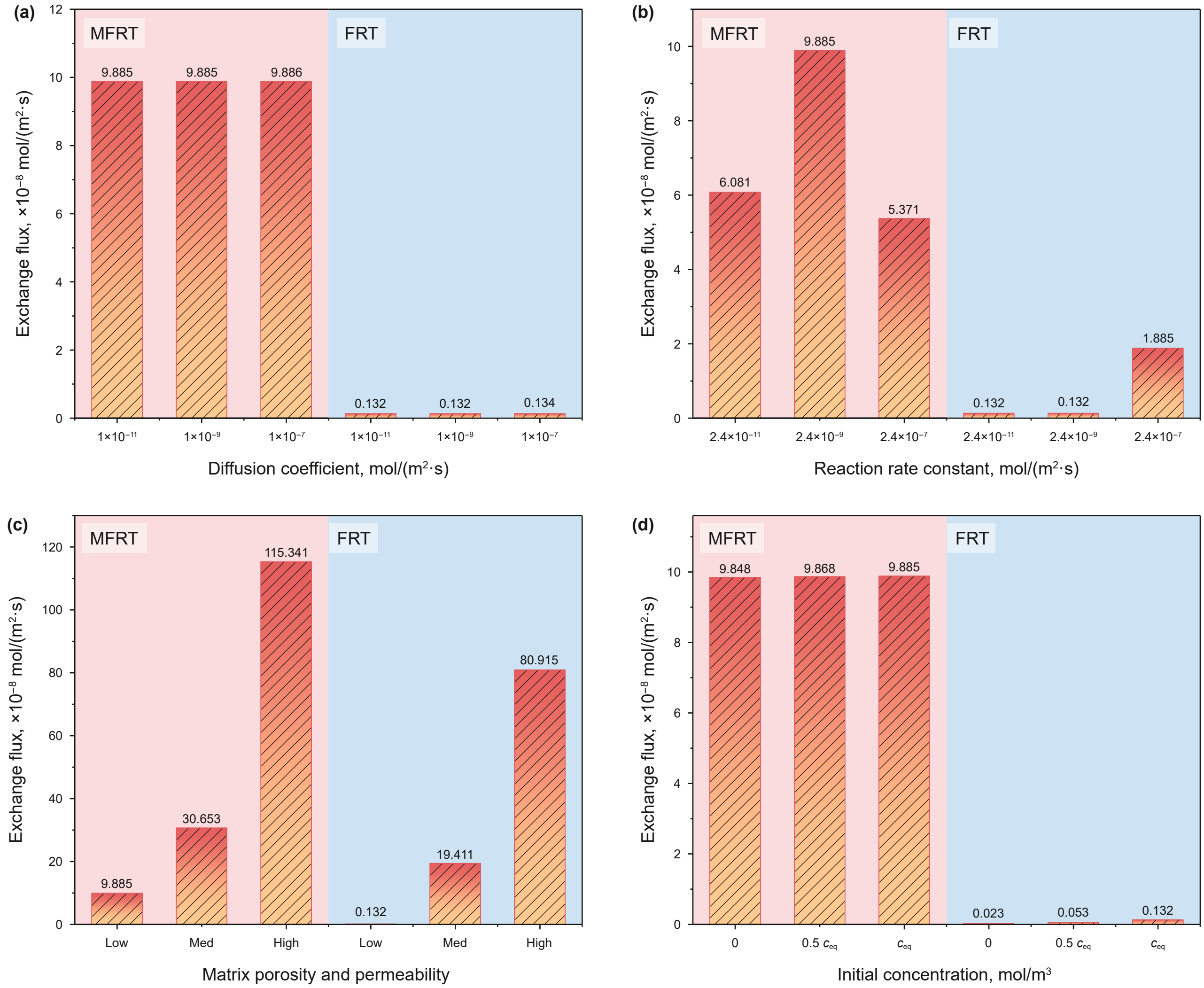

Fig. 10. Comparisons of exchange fluxes between fractures and matrix pores under different influence factors over 30 years of production, **(a)** diffusion coefficients; **(b)** reaction rate constant; **(c)** matrix porosity and permeability; **(d)** initial concentration.

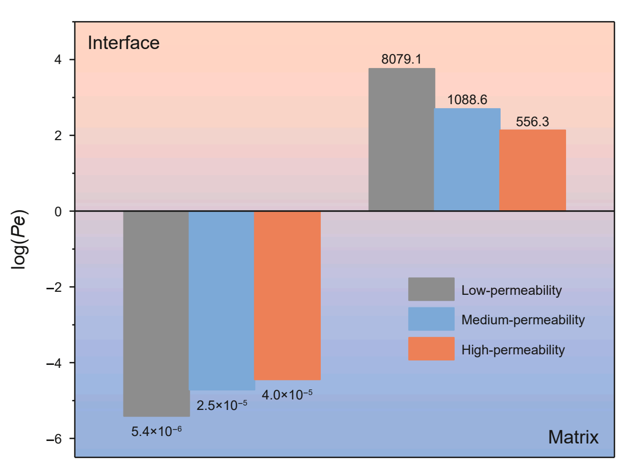

Fig. 11. The Peclet number for different diffusion coefficients (The log (Pe) is zero when the convection rate is equal to the diffusion rate, and the convection rate is greater than the diffusion rate when log (Pe) is greater than zero).

This indicates that mass transfer between fractures and matrix pores is convection-dominated, whereas that within the matrix is diffusion-dominated. Thus, solute transport away from fractures is diffusion-dominated and reactions stabilize once local equilibrium is reached, whereas near fractures advective exchange accelerates reactions and continually alters matrix permeability (Dhamu et al. 2024).

According to the above analysis, the extent to which various influencing factors affect the exchange fluxes varies between the MFRT case and the FRT case. Remarkably, under specific parameter settings, these factors act to reduce the differences in exchange fluxes between the two cases (Fig. 10(b) and (c)). This reduction in differences implies that the significance of MRT tends to decline under such particular parameter conditions. To quantitatively evaluate the effect of each influencing factor on the significance of MRT, the MFRT case is established as a benchmark. By comparing the deviation in exchange fluxes between the two cases, the significance of MRT was quantified. Take the diffusion coefficient as an example, when the diffusion coefficient is 1×10^{-9} mol/(m^2·s), the significance of MRT is calculated as (9.885 − 0.132)/9.885 = 98.67%.

Fig. 12 provides a visual comparison of how various factors affect the relative significance of MRT. Diffusion coefficients and initial concentrations exert relatively minimal influence on the significance of MRT (Fig. 12). As the diffusion coefficient increases from 1×10^{-11} to 1×10^{-7} mol/(m^2·s), the significance of MRT correspondingly decreases from 98.66% to 98.64% (Fig. 12(a)).

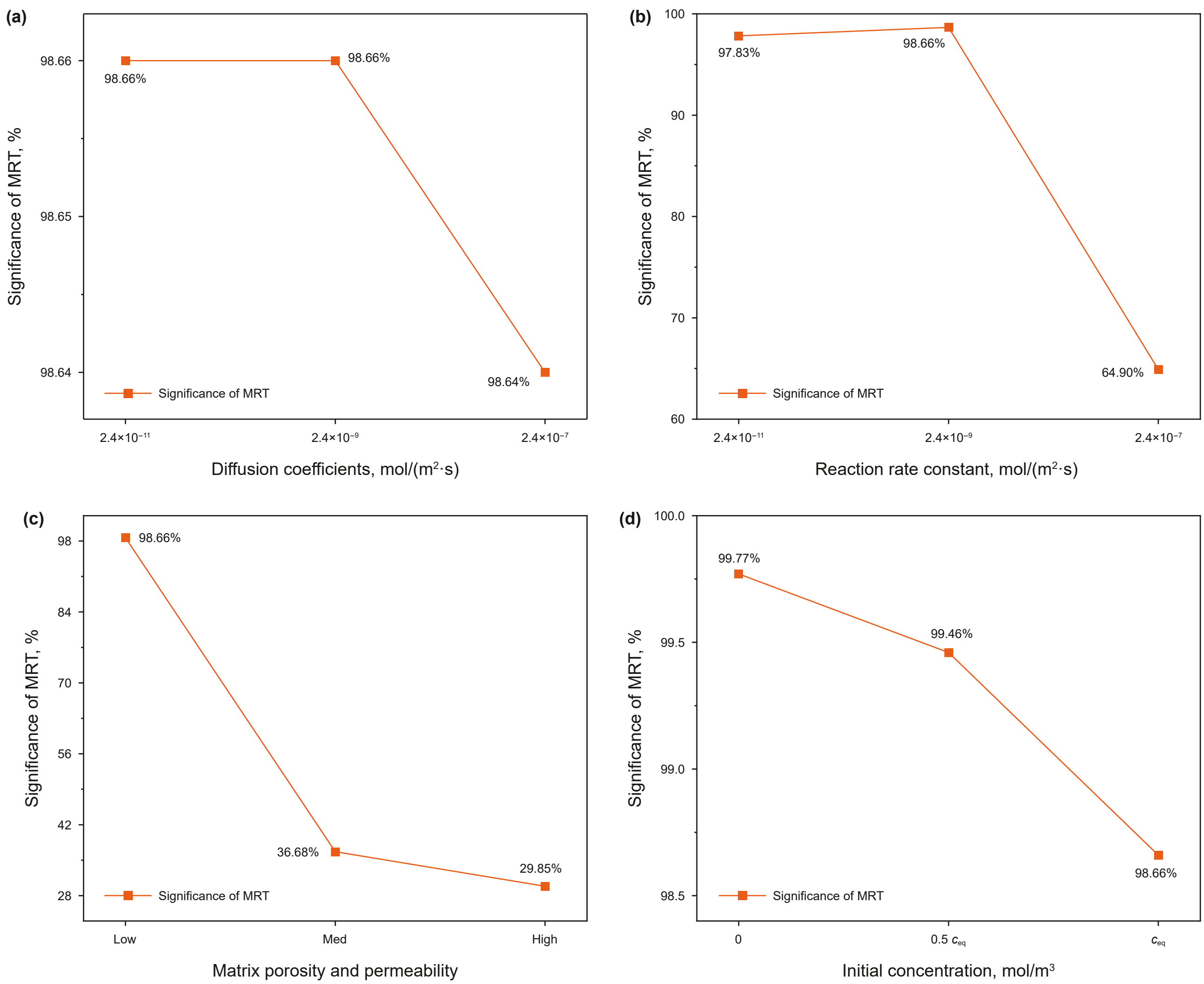

Fig. 12. The variation in the significance of MRT with influencing factors, **(a)** diffusion coefficients; **(b)** reaction rate constant; **(c)** matrix porosity and permeability; **(d)** initial concentration.

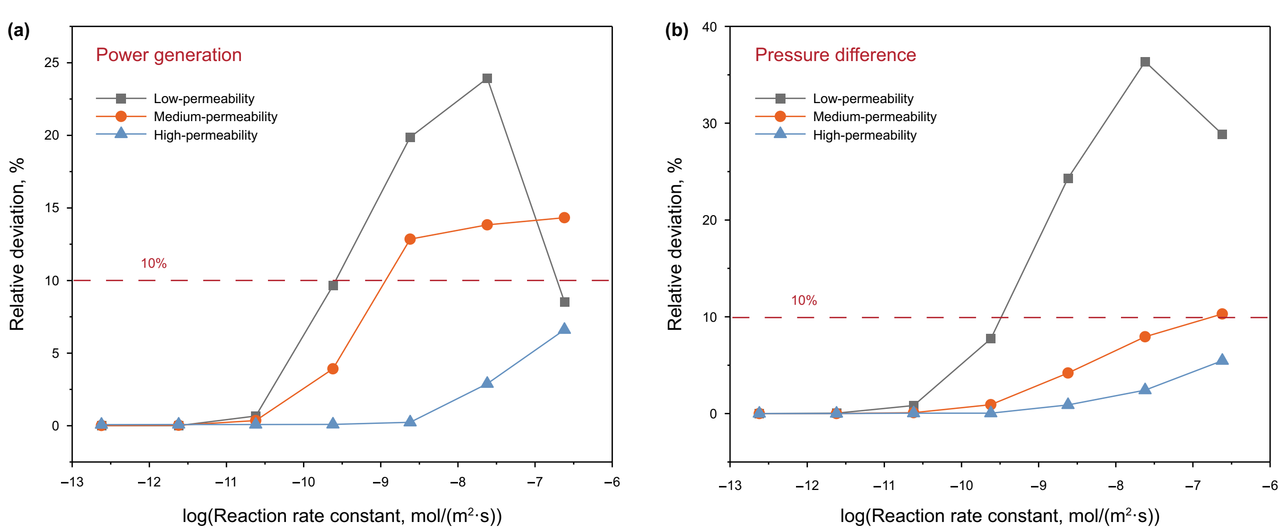

Fig. 13. Variation of relative deviation in **(a)** power generation and **(b)** pressure difference with reaction rate constants under different matrix porosity/permeability.

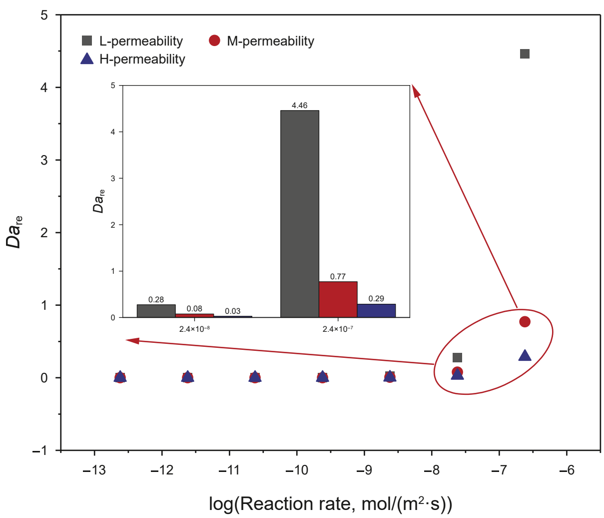

Fig. 14. Variation of Da_{re} with reaction rate constant for different matrix porosity/permeability.

Likewise, when the initial concentration is raised from 0 to saturated concentration, the significance of MRT diminishes from 99.77% to 98.66% (Fig. 12(d)). By contrast, reaction rate constants and matrix porosity and permeability significantly influence the significance of MRT. In particular, the significance of MRT drops significantly from 98.66% to 64.90% when the reaction rate constants rise from 2.4×10^{-9} to 2.4×10^{-7} mol/(m^2·s) (Fig. 12(b)). Similarly, the significance of MRT decreases dramatically from 98.66% to 29.85% when the matrix porosity and permeability change from low-permeability to high-permeability (Fig. 12(c)). From the above quantitative analyses, it is evident that matrix porosity and permeability, as well as reaction rate constants, are the key factors influencing the significance of MRT.

4.4. A criteria to evaluate the necessity of considering MRT in EGS modeling

The above analysis indicates that the significance of MRT varies significantly with changes in matrix porosity/permeability and reaction rate constants. Different types of fractured geothermal reservoirs might exhibit different MRT effects on heat extraction performance. In general, reactive transport processes in geothermal reservoirs are related to reservoir porosity/permeability characteristics, temperature, reactive mineral types, and reservoir solution concentration conditions. Reservoir temperature and reaction mineral type determine the mineral water-rock reaction rate constants, while reservoir solution concentration conditions determine the diffusion coefficient and solution saturation state. Our above analysis shows that the solution diffusion coefficient and saturation state are relatively minor factors in determining the significance of MRT. Thus, in this section, we primarily characterize different geothermal reservoir types by setting distinct porosity/permeability and mineral reaction rate constants. The common types of geothermal reservoirs are mainly classified into hot dry rock, karst reservoir, and sandstones (Xu et al. 2004, 2007; Holmslykke et al. 2017; Ji et al. 2024), representing low-permeability, medium-permeability, and high-permeability reservoirs respectively. The porosity and permeability are determined in accordance with section 4.3. Different types of geothermal reservoirs host different reactive minerals, primarily quartz, feldspar, and carbonate. The mineral water-rock reaction rate constants range from 10^{-13} to 10^{-7} mol/(m^2·s) (André et al. 2006; Ji et al. 2023a). It is worth noting that the porosity, permeability and reaction rate constants values set in this study cover nearly all reservoir types encountered in current medium and deep geothermal extraction.

The thermal performance in the MFRT case is employed as a benchmark, and the difference in thermal performance between the two cases (MFRT and FRT cases) is used to evaluate the significance of MRT. In low-permeability reservoir, the relative deviations in power generation and pressure difference first increase and then decrease, peaking at a reaction rate constant of 2.4×10^{-8} mol/(m^2·s). In contrast, in medium-permeability and high-permeability reservoirs, these relative deviations rise with the reaction rate constant. However, for the same reaction rate constant, the relative deviations decrease as the matrix porosity/permeability increase (Fig. 13). If a 10% deviation (typical engineering requirements) is adopted as the threshold to determine whether MRT needs to be considered, then for low-permeability reservoirs (hot dry rock), MRT should be considered when the reaction rate constant is between 2.4×10^{-10} and 2.4×10^{-7} mol/(m^2·s). For medium-permeability reservoir (karst), MRT should be considered when the reaction rate constant exceeds 2.4×10^{-9} mol/(m^2·s). As for high-permeability reservoirs (sandstones), MRT can be disregarded when the reaction rate constant ranges from 2.4×10^{-13} and 2.4×10^{-7} mol/(m^2·s).

In Fig. 13, an interesting phenomenon emerges: In low-permeability reservoirs, the relative deviations in thermal performance initially rise before falling, peaking at a reaction rate constant of 2.4×10^{-8} mol/(m^2·s). In contrast, these deviations show a monotonic increase in medium- and high-permeability reservoirs. To quantitatively explore this phenomenon, the Damkohler number (Menke et al. 2015; Peng et al. 2015) is employed to compare reaction and mass transfer rates at the matrix-fracture interface. $Da_{re} = k/Q_3$, where k denotes the reaction rate constant, mol/(m^2·s); Q_3 represents the exchange flux between matrix pores and fractures, mol/(m^2·s). It is well known that the reaction rate exceeds the mass transfer rate when Da_{re} is greater than one, and the effect of MRT on FRT is governed by the mass transfer between matrix pores and fractures. Conversely, when Da_{re} is less than one, this effect is dictated by water-rock reactions within the matrix pores near the fractures. Comparisons of Da_{re} values at the matrix-fracture interface under varying reaction rate constants and matrix porosity/permeability demonstrates that the Da_{re} increases with reaction rate and decreases with matrix porosity/permeability (Fig. 14). For low-permeability reservoirs, the Da_{re} exceeds one when the reaction rate constant reaches 2.4×10^{-7} mol/m^3. This indicates that the effect of MRT on FRT is governed by the mass transfer rate which is predominantly determined by the matrix porosity/permeability characteristics (Ling et al. 2022). Thus, the significance of MRT diminishes as the reaction rate constant increases from 2.4×10^{-8} to 2.4×10^{-7} mol/m^3 in low-permeability reservoirs. Conversely, for medium- and high-permeability reservoirs, the Da_{re} is less than one when the reaction rate constant ranges from 2.4×10^{-13} to 2.4×10^{-7} mol/(m^2·s). Here, the effect of MRT on FRT is dictated by the reaction rate constant, meaning the significance of MRT grows with increasing reaction rate constants in these reservoirs.

From the above analysis, it is evident that the effect of MRT on the system's heat extraction performance increases with the reaction rate and decreases with matrix porosity/permeability. However, if the reaction rate surpasses the mass transfer rate at the matrix-fracture interface, this effect will be diminished. Based on the results shown in Figs. 13 and 14, we conclude that when Da is less than or equal to one, the relative contribution of MRT increases progressively as the reaction rate constant increases. When the reaction rate approaches the mass-transfer rate at the matrix-fracture interfaces, MTR must be taken into account. By contrast, when *Da* exceeds one and the reaction rate surpasses the mass-transfer rate, reactions are effectively confined to fracture surfaces, and neglecting MTR is scientifically justified. During the extraction phase of conventional geothermal reservoirs, MRT must be considered for hot dry rocks, whose primary reacting minerals are quartz and feldspar, with mineral water-rock reaction rate constants range from 10^{-13} to 10^{-8} mol/(m^2·s). For karst geothermal reservoirs, the primary reactive minerals are dolomite and carbonate, with reaction rate constants on the order of 10^{-8} to 10^{-7} mol/(m^2·s), necessitating the consideration of MRT. However, for highly permeable sandstone geothermal reservoirs, the primary reactive minerals are carbonate and feldspar (Holmslykke et al. 2017), with reaction rate constants ranging from 10^{-13} to 10^{-7} mol/(m^2·s). Thus, MRT can be ignored in sandstone geothermal reservoirs.

5. Conclusions

In this study, the effect of MRT on fracture reactive transport and deformation, as well as on the system's heat-extraction performance, is systematically investigated using a fracture-pore dual-media THC coupled model. We find that matrix and fracture reactive transport compete, affecting fracture evolution and heat-extraction performance, and we demonstrate that MRT plays a significant role during the exploitation of HDR geothermal reservoirs. We further analyze how the significance of MRT depends on reaction-rate constants and matrix porosity/permeability. Drawing on the reaction rate constants and the porosity/permeability characteristics of conventional geothermal reservoirs, we assess the significance of MRT for the heat extraction from other fractured geothermal reservoir types. These key findings provide essential guidance for both the trade-off between accuracy and efficiency in geothermal production and the accurate assessment of fracture-pore structure evolution, as follows.

1. MRT significantly affects fracture deformation and thermal performance during HDR exploitation. In this study, neglecting MRT would underestimate the system's operational lifetime by 17 years and the pressure differential by 45.94%.
2. MRT acts by enhancing fracture-matrix exchange flux, which alters the concentration field in the fracture, thereby reducing the in-fracture reaction and deformation rates and ultimately affecting the heat-extraction performance in HDR systems.
3. Analysis of the dimensionless Damkohler number (*Da*, the ratio of reaction rate constant to fracture-matrix exchange fluxes) reveals that the significance of MRT increases with reaction rate constant when $Da < 1$ (reaction limited) and declines when $Da > 1$ (transport limited).
4. Based on reported reaction rate constants and the porosity and permeability characteristics of conventional geothermal reservoirs, we conclude that MRT is critical for heat extraction in HDR and karst reservoirs but negligible in sandstone reservoirs in this study.

Notably, this conclusion is derived from variations in porosity, permeability, and reaction rate constants. Consequently, it should apply to other settings analogous to those considered here, such as pollutant transport and CO_2 sequestration. Despite the encouraging theoretical results regarding the influence of MRT on fracture reactive transport, deformation, and system heat-extraction performance, substantial work remains to be done. First, our model operates at the field scale and cannot accurately resolve fracture-matrix mass transfer at the pore scale. Future work should employ pore-scale models or microfluidic experiments to further validate our conclusions (Cai et al. 2025). Additionally, our model omits stress effects (a 19.93% overestimation of the variation in average fracture aperture) and other mineral-water-rock interactions (a 28.6% underestimation of the overall reaction rate and a 16.5% reduction in fracture aperture evolution), which can materially affect estimates of system heat-extraction performance. We will refine the model in future work to enable more accurate evaluation of EGS heat-extraction performance. Given that water-rock reactions govern the long-term evolution of fracture morphology, we will investigate the effects of various chemical additives on the heat-extraction process, with the aim of achieving balanced heat extraction and extending system operational lifetime.

CRediT authorship contribution statement

Jia-Yan Ji: Writing – review & editing, Writing – original draft, Visualization, Validation, Methodology, Data curation, Conceptualization. **Hui Wu:** Writing – review & editing, Visualization, Software, Resources, Methodology. **Xian-Zhi Song:** Software, Resources, Funding acquisition.

Declaration of competing interest

The authors declare that they have no known competing financial interests or personal relationships that could have appeared to influence the work reported in this paper.

Acknowledgments

The authors would like to greatly acknowledge the National Natural Science Foundation of China (42372305), Postdoctoral Innovation Talent Support Program (BX20250030), National Key Research and Development Program of China (No. 2021YFA0716000), the China National Petroleum Corporation-Peking University Strategic Cooperation Project of Fundamental Research, the National Natural Science Fund for Major Program of China (Grant No. 52192624), and the National Science Fund for Distinguished Young Scholars of China (Grant No. 52125401).

Nomenclature

THMC	Thermal-hydraulic-mechanical-chemical
t	Time, s
u	Fluid velocity, m/s
k	Reservoir permeability, m^2
p	Pressure, Pa
d_f	Fracture aperture, m
g	Gravitational acceleration, m/s^2
T	Temperature, °C
$c_{p,f}$	Working fluid heat capacity, J/(kg·°C)
$c_{p,s}$	Heat capacity of the solid part in the reservoir, J/(kg·°C)
D_i	Effective diffusion coefficient of substance “i”, m^2/s
c_i	Concentration of substance “i”, mol/m^3
A_p	Specific surface areas of reservoir pores, 1/m
A_f	Specific surface areas of fracture, 1/m
f_c	Material transfer between matrix and fracture, dimensionless
R_i	Reaction rate of substance “i”, mol/(m^2·s)
R	Molar gas constant, J/(mol·K)
E_a	Reaction activation energy, kJ/mol
k^+	Reaction rate constants of carbonate, mol/(m^2·s)
SI	Saturation index, dimensionless
a_i	Activity of substance “i”, mol/m^3
K_{eq}	Equilibrium constant, dimensionless

d_h Hydraulic apertures, mm
d_{h0} Initial hydraulic apertures, mm
d_{f0} Initial fracture aperture, mm
f_f Transformation coefficient, dimensionless
T_{out} Production temperature, °C
T_{in} Injection temperature, °C
p_{in} Injection pressure, MPa
p_{out} Production pressure, MPa
Q_{in} Injection rate, kg/s
Q_{out} Production rate, kg/s
N Net thermal power, MW
K Hydraulic conductivity, m/s

Greek symbols

φ Porosity, dimensionless
μ_f Fluid dynamic viscosity, Pa·s
ρ_f Fluid density, kg/m^3
λ_s Heat conductivity of the solid part in the reservoir, W/(m·°C)
ρ_s Density of solid component of the reservoir, kg/m^3
λ_f Fluid heat conductivity, W/(m·K)
℧ Degree of unsaturation, dimensionless
Δp Injection-production pressure difference, MPa

References

Aminnaji, M., Qureshi, M.F., Dashti, H., et al., 2024. CO_2 gas hydrate for carbon capture and storage applications – part 2. Energy 300, 131580. https://doi.org/10.1016/j.energy.2024.131580.
Anderson, A., Rezaie, B., 2019. Geothermal technology: trends and potential role in a sustainable future. Appl. Energy 248, 18–34. https://doi.org/10.1016/j.apenergy.2019.04.102.
André, L., Rabemanana, V., Vuataz, F.-D., 2006. Influence of water–rock interactions on fracture permeability of the deep reservoir at Soultz-sous-Forêts, France. Geothermics 35, 507–531. https://doi.org/10.1016/j.geothermics.2006.09.006.
Blanc, P., Lassin, A., Piantone, P., et al., 2012. Thermoddem: a geochemical database focused on low temperature water/rock interactions and waste materials. Appl. Geochem. 27, 2107–2116. https://doi.org/10.1016/j.apgeochem.2012.06.002.
Cai, J., Yang, X., Yang, Z., et al., 2025. Microscopic flow and reactive transport in geological media: recent advances and challenges. Capillarity 17, 77–80. https://doi.org/10.46690/capi.2025.12.01.
Chen, Y., Ma, G., Wang, H., 2018. The simulation of thermo-hydro-chemical coupled heat extraction process in fractured geothermal reservoir. Appl. Therm. Eng. 143, 859–870. https://doi.org/10.1016/j.applthermaleng.2018.08.015.
Cheng, W., Wang, C., Nian, Y., et al., 2016. Analysis of influencing factors of heat extraction from enhanced geothermal systems considering water losses. Energy 115, 274–288. https://doi.org/10.1016/j.energy.2016.09.003.
Dhamu, V., Xiao, M., Qureshi, M., et al., 2024. Evaluating CO_2 hydrate kinetics in multi-layered sediments using experimental and machine learning approach: applicable to CO_2 sequestration. Energy 290, 129947. https://doi.org/10.1016/j.energy.2023.129947.
Gao, X., Yang, S., Tian, L., et al., 2024. System and multi-physics coupling model of liquid-CO_2 injection on CO_2 storage with enhanced gas recovery (CSEGR) framework. Energy 294, 130951. https://doi.org/10.1016/j.energy.2024.130951.
He, Y., Guo, Y., Jiang, Y., et al., 2025a. Hydraulic fracturing induced casing deformation and fault activation: from single-well fracturing to well-factory fracturing. Pet. Sci. 22, 4134–4144. https://doi.org/10.1016/j.petsci.2025.07.014.
He, Y., Guo, Y., Bi, Z., et al., 2025b. Study of field-scale carbon dioxide fracturing in hot dry rock reservoir based on a new 3D-THM coupled discrete block model. Geoenergy Sci. Eng. 247, 213675. https://doi.org/10.1016/j.geoen.2025.213675.
He, Y., Guo, Y., Yang, Z., et al., 2024. Integrated study of hydraulic/CO_2 fracturing and production coupled with a THM-D process in ultra-shallow shale reservoirs. Nat. Gas. Ind. B 11, 581–602. https://doi.org/10.1016/j.ngib.2024.09.001.
Holmslykke, H., Kjøller, C., Fabricius, I., 2017. Core flooding experiments and reactive transport modeling of seasonal heat storage in the hot deep gassum sandstone formation. ACS Earth Space Chem. 1 (5), 251–260. https://doi.org/10.1021/acsearthspacechem.7b00031.
Ji, J., Song, X., Yi, J., et al., 2024. Effects of pore water-rock reaction on heat extraction from the karst geothermal reservoirs: based on the dual media model. Energy 293, 130651. https://doi.org/10.1016/j.energy.2024.130651.
Ji, J., Zhao, J., Yi, J., et al., 2025. Optimization of hot dry rock heat extraction performance considering the interaction of multi-mineral component water-rock reactions and fracture roughness. Energy 320, 135089. https://doi.org/10.1016/j.energy.2025.135089.
Ji, J., Song, X., Li, S., et al., 2023a. Study on the effect of fracture morphology on fracture deformation based on the thermal-hydraulic-chemical-deformation coupling model. Energy 282, 128628. https://doi.org/10.1016/j.energy.2023.128628.
Ji, J., Song, X., Xu, F., et al., 2022. Effects of variable thermophysical properties of water on the heat extraction of an enhanced geothermal system: a numerical case study. Appl. Therm. Eng. 217, 119050. https://doi.org/10.1016/j.applthermaleng.2022.119050.
Ji, J., Song, X., Song, G., et al., 2023b. Study on fracture evolution model of the enhanced geothermal system under thermal-hydraulic-chemical-deformation coupling. Energy 269, 126604. https://doi.org/10.1016/j.energy.2022.126604.
Kang, F., Li, Y., Tang, C., et al., 2022. Competition between cooling contraction and fluid overpressure on aperture evolution in a geothermal system. Renew. Energy 186, 704–716. https://doi.org/10.1016/j.renene.2022.01.033.
Lei, Z., Zhang, Y., Zhang, S., et al., 2020. Electricity generation from a three-horizontal-well enhanced geothermal system in the Qiabuqia geothermal field, China: slickwater fracturing treatments for different reservoir scenarios. Renew. Energy 145, 65–83. https://doi.org/10.1016/j.renene.2019.06.024.
Li, G., Ji, J., Song, X., et al., 2022. Research advances in multi-field coupling model for geothermal reservoir heat extraction. Energy Rev., 100009 https://doi.org/10.1016/j.enrev.2022.100009.
Li, P., Li, D., Wang, Q., et al., 2021. Phase-field modeling of hydro-thermally induced fracture in thermo-poroelastic media. Eng. Fract. Mech. 254, 107887. https://doi.org/10.1016/j.engfracmech.2021.107887.
Ling, B., Sodwatana, M., Kohli, A., et al., 2022. Probing multiscale dissolution dynamics in natural rocks through microfluidics and compositional analysis. Proc. Natl. Acad. Sci. 119, e2122520119. https://doi.org/10.1073/pnas.2122520119.
Lu, S.M., 2018. A global review of enhanced geothermal system (EGS). Renew. Sustain. Energy Rev. 81, 2902–2921. https://doi.org/10.1016/j.rser.2017.06.097.
Lv, C., Tang, C., Zhu, C., et al., 2022. Environmental dependence of microbially induced calcium carbonate crystal precipitations: experimental evidence and insights. J. Geotech. Geoenviron. Eng. 148, 04022050. https://doi.org/10.1061/(asce)gt.1943-5606.0002827.
Lyu, X., Wang, W., Voskov, D., et al., 2025. Multiscale modeling for multiphase flow and reactive mass transport in subsurface energy storage: a review. Adv. Geo-Energy Res. 15, 245–260. https://doi.org/10.46690/ager.2025.03.07.
Maedo, M.A., Sánchez, M., Fabbri, H., et al., 2021. Coupled thermo-hydro-mechanical numerical modeling of evolving fractures in rocks. Rock Mech. Rock Eng. 54, 3569–3591. https://doi.org/10.1007/s00603-021-02387-1.
Menke, H.P., Bijeljic, B., Andrew, M.G., et al., 2015. Dynamic three-dimensional pore-scale imaging of reaction in a carbonate at reservoir conditions. Environ. Sci. Technol. 49, 4407–4414. https://doi.org/10.1021/es505789f.
Moslehi, S., Fazeli, H., Doster, F., et al., 2025. Development of a reactive transport solver in MATLAB reservoir Simulation Toolbox using the fully-implicit sequential iterative approach. Adv. Geo-Energy Res. 16, 114–130. https://doi.org/10.46690/ager.2025.05.04.
Ontoy, Y., Molling, P., Xu, T., et al., 2003. Scaling of hot brine injection wells: supplementing field studies with reactive transport modeling. Proceedings of TOUGH Symposium. https://api.semanticscholar.org/CorpusID:130176716.
Pandey, S.N., Chaudhuri, A., Kelkar, S., 2017. A coupled thermo-hydro-mechanical modeling of fracture aperture alteration and reservoir deformation during heat extraction from a geothermal reservoir. Geothermics 65, 17–31. https://doi.org/10.1016/j.geothermics.2016.08.006.
Pandey, S.N., Chaudhuri, A., Rajaram, H., et al., 2015. Fracture transmissivity evolution due to silica dissolution/precipitation during geothermal heat extraction. Geothermics 57, 111–126. https://doi.org/10.1016/j.geothermics.2015.06.011.
Peng, C., Crawshaw, J., Maitland, G.C., et al., 2015. Kinetics of calcite dissolution in CO_2-saturated water at temperatures between (323 and 373) K and pressures up to 13.8 MPa. Chem. Geol. 403, 74–85. https://doi.org/10.1016/j.chemgeo.2015.03.012.
Pruess, K., 2006. Enhanced geothermal systems (EGS) using CO_2 as working fluid—A novel approach for generating renewable energy with simultaneous sequestration of carbon. Geothermics 35, 351–367. https://doi.org/10.1016/j.geothermics.2006.08.002.
Qureshi, M.F., Khandelwal, H., Usadi, A., et al., 2022. CO_2 hydrate stability in oceanic sediments under brine conditions. Energy 256, 124625. https://doi.org/10.1016/j.energy.2022.124625.
Shi, Y., Cui, Q., Song, X., et al., 2023. Thermal performance of the aquifer thermal energy storage system considering vertical heat losses through aquitards. Renew. Energy 207, 447–460. https://doi.org/10.1016/j.renene.2023.03.044.
Song, G., Song, X., Xu, F., et al., 2022a. Contributions of thermo-poroelastic and chemical effects to the production of enhanced geothermal system based on thermo-hydro-mechanical-chemical modeling. J. Clean. Prod. 377, 134471. https://doi.org/10.1016/j.jclepro.2022.134471.
Song, G., Shi, Y., Xu, F., et al., 2024. The magnitudes of multi-physics effects on geothermal reservoir characteristics during the production of enhanced geothermal system. J. Clean. Prod. 434, 140070. https://doi.org/10.1016/j.jclepro.2023.140070.
Song, G., Song, X., Li, G., et al., 2021. An integrated multi-objective optimization method to improve the performance of multilateral-well geothermal system. Renew. Energy 172, 1233–1249. https://doi.org/10.1016/j.renene.2021.03.073.
Song, G., Song, X., Ji, J., et al., 2022b. Evolution of fracture aperture and thermal productivity influenced by chemical reaction in enhanced geothermal system. Renew. Energy 186, 126–142. https://doi.org/10.1016/j.renene.2021.12.133.

Song, X., Shi, Y., Li, G., et al., 2018. Numerical simulation of heat extraction performance in enhanced geothermal system with multilateral wells. Appl. Energy 218, 325–337. https://doi.org/10.1016/j.apenergy.2018.02.172.

Wang, C., Shi, X., Zhang, W., et al., 2022. Dynamic analysis of heat extraction rate by supercritical carbon dioxide in fractured rock mass based on a thermal-hydraulic-mechanics coupled model. Int. J. Min. Sci. Technol. 32, 225–236. https://doi.org/10.1016/j.ijmst.2021.12.004.

Wang, G., Wang, W., Zhang, W., et al., 2020. The status quo and prospect of geothermal resources exploration and development in Beijing-Tianj in-Hebei region in China. China Geol. 3, 173–181. https://doi.org/10.31035/cg2020013.

Wang, G., Zhang, W., Ma, F., et al., 2018. Overview on hydrothermal and hot dry rock researches in China. China Geol. 1, 273–285. https://doi.org/10.31035/cg2018021.

Wang, Y., Li, T., Chen, Y., et al., 2019. A three-dimensional thermo-hydro-mechanical coupled model for enhanced geothermal systems (EGS) embedded with discrete fracture networks. Comput. Methods Appl. Mech. Eng. 356, 465–489. https://doi.org/10.1016/j.cma.2019.06.037.

Wilson, J.L., Miller, P.J., 1978. Two-dimensional plume in uniform ground-water flow. J. Hydraul. Div. 104, 503–514. https://doi.org/10.1017/jfm.2021.1004.

Witherspoon, P., Amick, C.H., Gale, J.E., et al., 1979. Observations of a potential size effect in experimental determination of the hydraulic properties of fractures. Water Resour. Res. 15, 1142–1146. https://doi.org/10.1029/WR015i005p01142.

Xu, F., Song, X., Li, S., et al., 2024. A multi-objective optimization and multi-attribute decision-making analysis for technical-thermodynamic-economic evaluation considering the rock damage on production performance of hot dry rock geothermal resources. Appl. Therm. Eng. 241, 122350. https://doi.org/10.1016/j.applthermaleng.2024.122350.

Xu, T., Apps, J.A., Pruess, K., et al., 2007. Numerical modeling of injection and mineral trapping of CO_2 with H_2S and SO_2 in a sandstone formation. Chem. Geol. 242, 319–346. https://doi.org/10.1016/j.chemgeo.2007.03.022.

Xu, T., Ontoy, Y., Molling, P., et al., 2004. Reactive transport modeling of injection well scaling and acidizing at Tiwi field, Philippines. Geothermics 33, 477–491. https://doi.org/10.1016/j.geothermics.2003.09.012.

Xu, T., Hu, Z., Li, S., et al., 2018. Enhanced geothermal system: international progresses and research status of China. Acta Geol. Sin. 92, 1936–1947. https://doi.org/10.3969/j.issn.0001-5717.2018.09.012 (in Chinese).

Yang, R., Wang, Y., Song, G., et al., 2023. Fracturing and thermal extraction optimization methods in enhanced geothermal systems. Adv. Geo-Energy Res. 9, 136–140. https://doi.org/10.46690/ager.2023.08.07.

Ye, Z., Wang, J., 2020. A thermal-hydraulic-mechanical coupling study of heat extraction from the geothermal reservoir with a discrete fracture network. Geofluids, 8875918. https://doi.org/10.1155/2020/8875918.

Zhu, J., Hu, K., Lu, X., et al., 2015. A review of geothermal energy resources, development, and applications in China: current status and prospects. Energy 93, 466–483. https://doi.org/10.1016/j.energy.2015.08.098.